

Optical properties of Bi₂Te₂Se at ambient and high pressuresAna Akrap,^{*} Michaël Tran, Alberto Ubaldini, Jérémie Teyssier, Enrico Giannini, and Dirk van der Marel
*University of Geneva, CH-1211 Geneva 4, Switzerland*Philippe Lerch
*Paul Scherrer Institute, CH-5232 Villigen, Switzerland*Christopher C. Homes[†]*Condensed Matter Physics and Materials Sciences Department, Brookhaven National Laboratory, Upton, New York 11973, USA*
(Received 24 September 2012; revised manuscript received 3 December 2012; published 26 December 2012)

The temperature dependence of the complex optical properties of the three-dimensional topological insulator Bi₂Te₂Se is reported for light polarized in the *a-b* planes at ambient pressure, as well as the effects of pressure at room temperature. This material displays a semiconducting character with a bulk optical gap of $E_g \simeq 300$ meV at 295 K. In addition to the two expected infrared-active vibrations observed in the planes, there is an additional fine structure that is attributed to either the removal of degeneracy or the activation of Raman modes due to disorder. A strong impurity band located at $\simeq 200$ cm⁻¹ is also observed. At and just above the optical gap, several interband absorptions are found to show a strong temperature and pressure dependence. As the temperature is lowered these features increase in strength and harden. The application of pressure leads to a very abrupt closing of the gap above 8 GPa, and strongly modifies the interband absorptions in the midinfrared spectral range. While *ab initio* calculations fail to predict the collapse of the gap, they do successfully describe the size of the band gap at ambient pressure, and the magnitude and shape of the optical conductivity.

DOI: [10.1103/PhysRevB.86.235207](https://doi.org/10.1103/PhysRevB.86.235207)

PACS number(s): 72.20.-i, 78.20.-e, 74.62.Fj

I. INTRODUCTION

A topological insulator is a material in which a large spin-orbit interaction produces a band inversion over a bulk band gap, resulting in protected metallic surface states.¹⁻³ In the search for three-dimensional topological insulators, the discovery of the layered bismuth chalcogenide Bi₂Te_{3-x}Se_x family was of particular importance.^{4,5} The simple structure of the surface states in these compounds, with only one Dirac cone traversing the band gap,^{6,7} has attracted a great deal of interest. The suitably sized bulk band gap (150–300 meV) and robust metallic surface states persisting up to high temperatures⁷ make this series of compounds interesting for experimental investigation, and potentially also in applications. However, difficulties concerning material purity and stoichiometry lead to a deteriorated insulating character of the bulk. Bismuth and tellurium have very similar electronegativity on Pauling's scale,⁸ and this naturally leads to a large concentration of antisite defects. Bi₂Te₃ is not a line compound but exists in a narrow field of compositions ($\sim 1\%$);⁹ as a result, a slight deficiency or excess of Te will result in either a *p*-type or *n*-type material, respectively.¹⁰ Very often it is the case that Bi₂Te₃ crystals are *p* type and have a high hole concentration because of a large number of negatively charged defects due to tellurium sites occupied by bismuth atoms.¹¹ In Bi₂Se₃, on the other hand, because of the high fugacity of selenium, the concentration of selenium vacancies exceeds the concentration of antisite defects, so that the Bi_{2+x}Se₃ crystal typically exhibits *n*-type conductivity.^{12,13} All of these factors cause disorder (impurities) in the structure and lead to symmetry breaking and intrinsic doping. Contrary to the expected insulating state, a finite residual conductivity appears. The salient question is how to optimize these systems and decrease the bulk conductivity.

In an ordered stoichiometric structure Se vacancies can be decreased, and the Se/Te randomness diminished. Recently, it was found that Bi₂Te₂Se has the highest resistivity within the Bi₂Te_{3-x}Se_x family. Shubnikov-de Haas oscillations were observed and attributed to the surface states,¹⁴⁻¹⁷ and a single Dirac cone crosses the Fermi surface.¹⁸ Angle-resolved photoemission spectroscopy (ARPES) shows narrow linewidths of topological surface states, which indicates that the disorder is suppressed.^{19,20}

To improve existing topological insulators and design new ones, it is necessary to understand the details of their band structure. It is important to know how the impurities influence the conductivity, and what happens if the lattice dimensions are varied, for example, through chemical substitutions. Much of this can be addressed through a careful study of the optical properties. The optical properties of Bi₂Te₃ and Bi₂Se₃ crystals have been intensely studied in the past century.²¹ More recently, this family of compounds has been revisited in light of the topological properties.^{22,23} In this paper we focus on Bi₂Te₂Se and investigate the temperature dependence of the complex optical properties to improve the understanding of the bulk response. Through room-temperature reflection and transmission experiments at ambient and high pressure, information is obtained about the nature of the band gap, residual conductivity, vibrational modes, and interband transitions. The application of pressure allows the band gap to be studied as the distance between the layers is decreased.

We observe a semiconducting response in the optical conductivity of Bi₂Te₂Se with a gap of $E_g \simeq 2400$ cm⁻¹ (0.3 eV); below the gap are two strong infrared-active phonons at $\simeq 62$ and 118 cm⁻¹, an impurity band centered at $\simeq 200$ cm⁻¹, as well as other weaker features. In addition, there is evidence of a low-energy impurity band at 30 – 40 cm⁻¹, in agreement with a small transport gap extracted from the

dc conductivity measurement. The low-energy interband absorptions display a pronounced temperature dependence. The application of pressure with a diamond-anvil cell in $\text{Bi}_2\text{Te}_2\text{Se}$ reduces the interlayer spacing, altering the band structure. The optical gap is at first unchanged, and then strongly reduced upon pressure increase. Reflectance studies reveal that the band structure is altered by the application of even a small amount of pressure. *Ab initio* calculations of the electronic structure and the optical conductivity confirm the sensitivity of interband absorptions to *c*-axis compression. However, the calculations show that *c*-axis compression has very little effect on the band gap.

II. EXPERIMENT AND CALCULATION

Single crystals of $\text{Bi}_2\text{Te}_2\text{Se}$ were grown by the floating zone method starting from the stoichiometric ratio of metallic bismuth and chalcogenide elements. Cleaving the crystal exposes lustrous mirror-like surfaces, which flake off very easily.

The structure of $\text{Bi}_2\text{Te}_2\text{Se}$ is described by the trigonal space group $R\bar{3}m$ (kawazulite) and shown in the inset of Fig. 1. The unit cell consists of quintuple Te–Bi–Se–Bi–Te layers stacked along the *c*-axis direction.^{24,25} The quintuple layers are bound by weak van der Waals interaction, which is responsible for the extreme ease with which the sample may be cleaved.

The temperature-dependent reflectance at ambient pressure was measured at a near-normal angle of incidence on a freshly cleaved surface for light polarized in the *a*-*b* planes, from $\simeq 12$ to over $42\,000\text{ cm}^{-1}$ (1.5 meV – 5.2 eV) using an *in situ* evaporation technique.²⁶ The reflectance is a complex quantity, $\tilde{r} = \sqrt{R}e^{i\theta}$; however, only the amplitude R is measured in this experiment. To obtain the phase we employ the Kramers-Kronig relation²⁷ using suitable extrapolations for the reflectance in the $\omega \rightarrow 0, \infty$ limits. At low frequencies the metallic Hagen-Rubens form for the reflectance $R(\omega) \propto 1 - \sqrt{\omega}$ is employed. Above the highest measured frequency point the reflectance is assumed to be constant up to $\simeq 8 \times$

10^4 cm^{-1} , above which a free electron gas asymptotic reflectance extrapolation $R(\omega) \propto 1/\omega^4$ is assumed.²⁸

Raman spectra were collected using a homemade micro Raman spectrometer equipped with an argon laser at a wavelength of 514.5 nm , a half-meter monochromator, and a liquid nitrogen-cooled CCD detector. The spectral resolution was of the order of 1 cm^{-1} . The sample was mounted in a helium-flow cryostat allowing measurements down to 6 K with a long working distance $63\times$ objective.

Optical data at high pressure were recorded using a diamond-anvil cell operated in transmission and reflection geometry. Type IIa diamonds with a culet of 0.55 mm were used with CuBe gaskets with a hole diameter of $250\text{ }\mu\text{m}$ to apply pressures of up to 15 GPa inside a membrane-driven diamond-anvil cell. Samples of $\text{Bi}_2\text{Te}_2\text{Se}$ were cleaved to a thickness of a few microns. A fine dry KBr powder was used as the pressure-transmitting medium, and the pressure was monitored *in situ* through ruby fluorescence.²⁹ In the transmission geometry, light is focused on the sample in a homemade transmission setup with a pair of reflective objectives with a magnification coefficient of 15 and numerical aperture 0.5 . For the reflectivity measurement, a Bruker Hyperion 3000 microscope was used with a single $15\times$ reflective objective. Infrared radiation was provided by the Swiss synchrotron light source (SLS) and coupled³⁰ to the Fourier transform spectrometer. The high-brightness provided by the synchrotron source allows a spatial resolution of $30 \times 30\text{ }\mu\text{m}^2$ or better while maintaining high throughput.

The band structure was calculated for the primitive cell containing five atoms. We used a full-potential linear muffin-tin-orbital (LMTO) program³¹ within a local spin-density approximation (LSDA) and generalized gradient approximation (GGA).³² The effect of spin-orbit coupling was taken into account.^{33,34} The k mesh was $40 \times 40 \times 40$ for the self-consistency calculation, and $12 \times 12 \times 12$ for the calculation of the optical conductivity. The energy cutoff was set at 730 eV , and the convergence criterium is such that the total energy accuracy is better than 10^{-6} eV .

III. RESULTS AND DISCUSSION

The resistivity measured in the *a*-*b* plane is shown in Fig. 1 in an Arrhenius plot ($\log \rho_{ab}$ against $1/T$). At 5 K , $\rho_{ab} \simeq 0.16\text{ }\Omega\text{ cm}$. From room temperature down to $\sim 170\text{ K}$ the behavior of the resistivity is similar to that of a bad metal. The value of ρ_{ab} at room temperature is $\simeq 16\text{ m}\Omega\text{ cm}$, and the temperature slope is small and positive, $\simeq 1.3 \times 10^{-5}\text{ }\Omega\text{ cm/K}$. Between 170 and 30 K we see activated behavior with the transport gap $E_g \simeq 5\text{ meV}$; a fit to the activated behavior is shown in Fig. 1. At the lowest temperatures the gap appears to decrease down to $\simeq 0.43\text{ meV}$, pointing to a contribution from activation of donor (acceptor) levels, and the metallic surface states. In comparison with previously reported results,^{14,15} our sample has a smaller activation energy; previous reports are in the range 20 – 23 meV . The residual resistivity at low temperatures is 10 – 50 times smaller than in previous reports.^{14,15} However, the transport gaps observed in other works in the $T \rightarrow 0\text{ K}$ limit are much smaller, $\simeq 4\text{ }\mu\text{eV}$, hinting at a more significant contribution from activation of donor/acceptor levels and the surface states

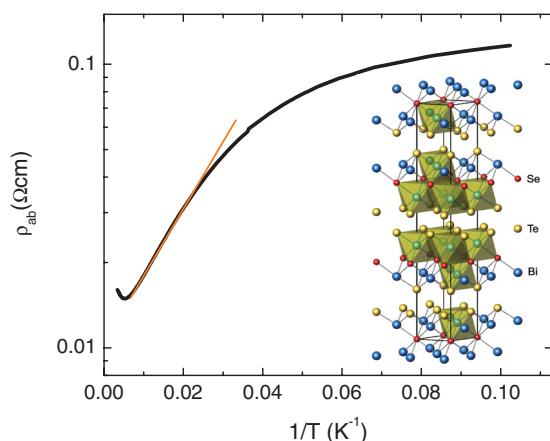


FIG. 1. (Color online) Arrhenius plot of the in-plane resistivity of $\text{Bi}_2\text{Te}_2\text{Se}$, $\log \rho$ vs $1/T$. The straight line is a fit to the activated hopping formula, $\rho = \rho_0 \exp[E_g/(k_B T)]$, between 30 and 170 K . Inset: The unit cell illustrating the quintuple Te–Bi–Se–Bi–Te layers stacked along the *c* axis.

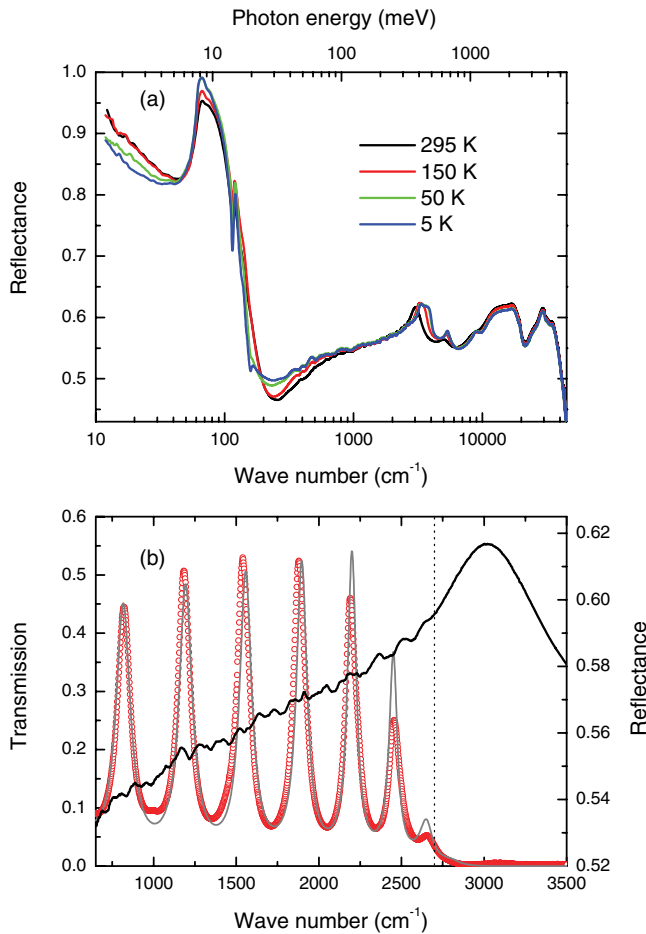


FIG. 2. (Color online) (a) Reflectivity of Bi₂Te₂Se over a wide frequency range for light polarized in the *a-b* planes at several temperatures. (b) Transmission through a cleaved flake $\approx 2\text{-}\mu\text{m}$ thick compared to the bulk reflectance at 295 K. Open red symbols are the measured values of transmission, and the thin gray line is fit using the Tauc-Lorentz model. The dotted line indicates the point at which the sample becomes opaque.

than in our sample. The difference in transport properties is probably related to minute stoichiometry differences. The measurement of thermopower on a sample from the same batch showed that the charge carriers in the sample are electrons.³⁵

A. Energy gap

The temperature dependence of the reflectance of Bi₂Te₂Se for the light polarized in the *a-b* plane is shown over a wide frequency range in Fig. 2(a); the region close to the band edge is shown in more detail in Fig. 2(b) at 295 K. The reflectance in the far infrared displays a weakly metallic character and is dominated by a strong low-frequency phonon mode. A weaker phonon mode can be distinguished above 100 cm⁻¹ as a small notch superimposed on the stronger feature. At higher energies structures due to the gap edge at $E_g \approx 300$ meV and several interband transitions are clearly visible in the reflectance. In addition, some of these features have a pronounced temperature dependence.

The real part of the optical conductivity (σ_1) has been determined from a Kramers-Kronig analysis of the reflectance

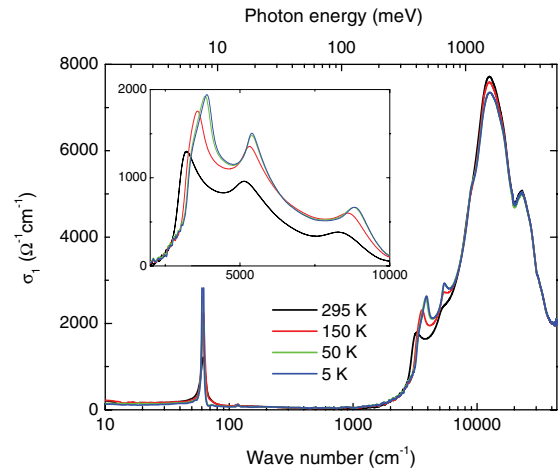


FIG. 3. (Color online) Optical conductivity in the planes of Bi₂Te₂Se over a wide energy range for several different temperatures. Inset: Optical conductivity in the midinfrared and near-infrared regions with the contribution from the high-frequency oscillators removed.

and is shown over a wide range in Fig. 3. The most prominent features are the strongly temperature-dependent interband absorptions associated with the band edge and a very strong low-energy vibration at ≈ 62 cm⁻¹. From σ_1 the optical band gap can be roughly estimated to $E_g \approx 2400$ cm⁻¹ (300 meV) at 295 K. The onset of the gap in Bi₂Te₂Se is much sharper than in Bi₂Se₃ (Ref. 22), where the natural Se deficiency results in intrinsic doping and a well-defined metallic (Drude-like) contribution. It may be noted that the transport gap extracted from the resistivity measurement is almost two orders of magnitude smaller than the optical band gap, which suggests that conduction occurs as a result of hopping through localized impurity states within the gap.

An improved estimate of the band gap may be obtained from combining the reflectance and transmission measurements. A comparison of the reflectance of the bulk material and the transmission through a thin sample at 295 K is shown in Fig. 2(b). Strong Fabry-Perot oscillations are observed in the transmission in the midinfrared region; however, weak fringes are also observed in the reflectance. The explanation for this is that the sample cleaves extremely easily and its surface inevitably terminates in thin flakes. A part of the incident light is reflected while another part is transmitted through the flake and reflected from the back surface; the back reflection interferes with the primary reflection and produces fringes. A dashed vertical line at 2700 cm⁻¹ (335 meV) indicates where the Fabry-Perot oscillations in both the reflectance and transmission appear to terminate. The transmission data have been fit using a Tauc-Lorentz model³⁶ for the dielectric function in which a modified Lorentzian oscillator [see Eq. (2)] is used to describe the interband absorptions; the imaginary part is written as

$$\epsilon_{2,TL} = \begin{cases} \left[\frac{A\Gamma\omega_0(\omega - E_g/\hbar)^2}{(\omega^2 - \omega_0^2)^2 + \Gamma^2\omega^2} \cdot \frac{1}{\omega} \right], & \hbar\omega > E_g, \\ 0, & \hbar\omega \leq E_g. \end{cases} \quad (1)$$

The fitted parameters A , Γ , $\hbar\omega_0$, and E_g correspond to the intensity, broadening, transition energy, and energy gap,

respectively. The real part is determined from a Kramers-Kronig analysis of $\epsilon_{2,TL}$, allowing the transmission to be calculated for a thin slab.³⁷ Pieces of varying thickness ($\simeq 0.8$ – $9 \mu\text{m}$) have been examined, and the fit to the transmission through a $2\text{-}\mu\text{m}$ -thick flake of $\text{Bi}_2\text{Te}_2\text{Se}$ is shown in Fig. 2(b). The band gap was determined in samples with several different thicknesses to be $E_g \approx 285 \text{ meV}$ [$E_g/(2\pi\hbar c) \approx 2300 \text{ cm}^{-1}$], which is somewhat lower than the energy at which the fringes are observed to disappear.

The optical properties of the bulk are described using the Drude-Lorentz model for the complex dielectric function

$$\tilde{\epsilon}(\omega) = \epsilon_\infty - \frac{\omega_{pD}^2}{\omega^2 + i\omega/\tau_D} + \sum_j \frac{\Omega_j^2}{\omega_j^2 - \omega^2 - i\omega\gamma_j}, \quad (2)$$

where ϵ_∞ is the real part of the dielectric function at high frequency, $\omega_{p,D}^2 = 4\pi ne^2/m^*$ and $1/\tau_D$ are the square of the plasma frequency, and the scattering rate for the delocalized (Drude) carriers, respectively, and m^* is an effective mass. For the Lorentz oscillators ω_j , γ_j , and Ω_j represent the position, width, and strength of the j th vibration or excitation. The complex conductivity is $\tilde{\sigma} = \sigma_1 + i\sigma_2 = -i\omega[\tilde{\epsilon}(\omega) - \epsilon_\infty]/4\pi$. In addition to the vibrational parameters, discussed in Sec. III B, a fit to the low-frequency conductivity at room temperature yields $\omega_{pD} \simeq 1300 \text{ cm}^{-1}$ and $1/\tau_D \simeq 200 \text{ cm}^{-1}$; this value for the plasma frequency corresponds to a carrier concentration of $n/m^* \simeq 1.7 \times 10^{18} \text{ cm}^{-3}$, consistent with previous results.¹⁰

One of the more interesting aspects of this material is the unusual temperature dependence of the interband transition associated with the gap edge, shown in Fig. 3, in which the increase in intensity, or spectral weight (defined as the area under the conductivity curve over a given frequency interval) of this feature, or set of features, in the 2500 – 7000 cm^{-1} region, is compensated for by a loss of spectral weight at high frequency. This behavior may be shown in more detail by fitting the strong high-frequency features at $\simeq 13000$ and 24000 cm^{-1} and then subtracting this contribution from the conductivity. The result of this procedure is shown in the inset of Fig. 3. At low temperature the peak of the lowest interband absorption hardens by $\simeq 700 \text{ cm}^{-1}$ and develops a weak shoulder, while the two higher-energy features appear symmetric and display smaller blue shifts. The gap edge appears to harden by $\simeq 430 \text{ cm}^{-1}$.

The thermal shifts in the gap edge and the absorption peaks are significant. One effect of the decrease in temperature is that the lattice contracts, which leads to an increase in the band gap.³⁸ However, a more important process is the phonon absorption and re-emission. The highest-energy phonons in the system (Sec. III B) set a temperature scale of approximately 170 K . When the temperature is much lower than this, the phonon processes become inaccessible and the gap increases. While the strong temperature dependence of the gap may be understood with phonons, the unusual shifts of the interband absorptions are more likely linked to the contraction of the lattice.

At long wavelengths the optical conductivity is consistent with the dc transport: the conductivity is very small and it further decreases as temperature is lowered. As shown in Fig. 4(a), the values of σ_1 extrapolate roughly to the values of the dc conductivity. Since the dc conductivity

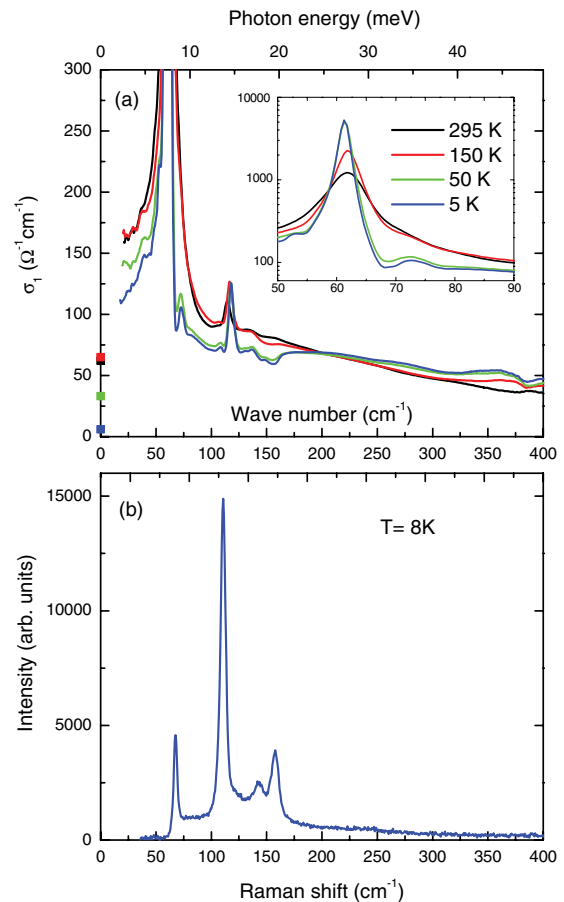


FIG. 4. (Color online) (a) The temperature dependence of the real part of the optical conductivity of $\text{Bi}_2\text{Te}_2\text{Se}$ for light polarized in the planes at low energies. The symbols at the origin denote the transport values for the dc conductivity. Inset: The conductivity in the region of the strong optical phonon showing the asymmetry in the feature at low temperature. (b) The Raman response at 8 K .

at low temperatures is finite, there is also a weak free-carrier (Drude-like) contribution. However, it is impossible to accurately model this since it is masked by larger effects; a strong background which peaks around the 62 cm^{-1} phonon and persists up to at least 400 cm^{-1} . A part of this broad background may be identified as a far-infrared band due to the presence of impurities. The impurity band is slightly enhanced as the temperature is lowered. This is in agreement to what was previously reported in $\text{Bi}_2\text{Te}_2\text{Se}$ and attributed to impurities.²³ A similar impurity band was also observed several years ago in a series of doped semiconductors, Si:P (Ref. 39). The presence of impurity states in the low-energy excitations agrees with the small transport gap obtained from the resistivity measurement. A wide impurity band is centered at 200 – 300 cm^{-1} , but there may be another impurity band centered at 30 – 40 cm^{-1} (~ 4 – 5 meV), lying in the side band of the strong optical phonon. While this last impurity band would agree with the small activation energy obtained in the resistivity measurement, it is possible that this feature is instead linked to the strong low-lying E_u phonon, discussed in the following section.

B. Vibrational properties

The optical conductivity of Bi₂Te₂Se allows the vibrational properties to be analyzed. As Fig. 4(a) shows, only two sharp phonon peaks are observed at room temperature. At low temperatures these vibrations further sharpen, but in addition several other, albeit much weaker, modes appear. The symmetry group analysis of Bi₂Te₂Se in the $R\bar{3}m$ setting gives the irreducible vibrational representation^{21,40}

$$\Gamma_{\text{vib}} = 2A_{1g} + 2E_g + 2A_{2u} + 2E_u. \quad (3)$$

Here, the A_{1g} and E_g modes are Raman active. The A_{2u} and E_u modes are infrared active along the c axis and the a - b planes, respectively. The two E_u modes can be identified as the two strong vibrations observed at 62 cm⁻¹ and 117 cm⁻¹ (Ref. 41). As the temperature is decreased, the low-energy mode softens, while the higher-energy mode hardens. At low temperatures the 62 cm⁻¹ mode, shown in the inset of Fig. 4(a), appears to develop a slight asymmetry, with a tail at low frequencies. An inhomogeneous structure would be enough to cause an asymmetry in such a strong phonon mode; however, small level shifts in the reflectance can also artificially produce an asymmetry in the line shape of a strong phonon in an insulator.

The infrared-active modes observed at 5 K have been fit to Lorentz oscillators with a polynomial background and the frequencies, widths, and strengths are listed in Table I. Contrary to previous experiments on Bi₂Se₃ (Ref. 22), we can find no convincing evidence of Fano-like behavior in the strong phonon at $\simeq 62$ cm⁻¹. In addition to the two allowed in-plane infrared modes, there are at least seven other infrared-active modes observed. It is possible that disorder may lead to the lifting of the degeneracy of the E_u modes, leading to weak splitting. However, we note that the fit to

TABLE I. The fitted parameters for the infrared-active modes in the optical conductivity at 5 K and the Raman-active modes at 8 K. The estimated errors are indicated in parentheses. With the exception of the Raman intensities, all units are cm⁻¹.

Infrared ^a			
Mode	ω_j	γ_j	Ω_j
E_u	51.6 (0.1)	8.3 (0.7)	133 (11)
	61.7 (0.03)	2.0 (0.1)	936 (25)
	72.7 (0.04)	7.0 (0.3)	114 (4)
	108.0 (0.1)	6.1 (0.7)	40 (4)
E_u	117.8 (0.02)	6.0 (0.1)	159 (2)
	137.1 (0.08)	8.5 (0.5)	55 (2)
	149.0 (0.09)	5.0 (0.5)	22 (2)
	(Antiresonance ^b)		
	144.1 (0.1)	9.0 (0.5)	68 (3)
	155.8 (0.1)	13.1 (0.8)	100 (4)
Raman			
Mode	ω_j	γ_j	I/I_0
A_{1g}/E_g	67.7 (0.1)	3.5 (0.2)	0.21
A_{1g}/E_g	110.7 (0.1)	5.1 (0.1)	1.00
A_{1g}/E_g	142.2 (0.5)	19.6 (3.5)	0.35
A_{1g}/E_g	157.7 (0.2)	7.1 (0.4)	0.27

^aTwo very weak modes at ≈ 39 and 85 cm⁻¹ are identified but not fit.

^bThe modes at 137.1 and 149 cm⁻¹ are fit using antiresonances.

the conductivity by employing two resonances at $\simeq 137$ and 149 cm⁻¹ may actually be improved by considering two Fano antiresonances⁴² at $\simeq 144.1$ and 155.8 cm⁻¹, respectively. The Raman spectrum is shown at 8 K in Fig. 4(b). The energies of the Raman-active modes are very close to the energies of some of the weak phonons that appear in the conductivity at low temperature; it is possible that symmetry breaking may lead to the activation of Raman modes that are normally not infrared active. In particular the positions of the two antiresonances in the conductivity are very close to the two high-frequency Raman modes at 142 and 158 cm⁻¹ (Table I). In low-dimensional materials, the totally symmetric A_{1g} Raman modes have been observed to undergo out-of-phase coupling to produce an optically active mode at the same frequency as the Raman mode;⁴³ in systems where these modes sit upon a strong electronic background they appear as antiresonances rather than resonances.⁴⁴ A similar mechanism may be responsible for the Fano-like line shapes observed in this material. Since we seem to observe at least nine modes in total, it is also possible that the A_{2u} out-of-plane modes may also be activated by disorder or a slight misalignment; these vibrations typically manifest themselves in the planes at the longitudinal-optic positions.⁴⁵ Overall, the low-energy optical and vibrational properties of Bi₂Te₂Se point towards the importance of substitutional disorder and intrinsic doping.

C. Pressure

The structure of Bi₂Te₂Se appears to be “soft” or easily compressible along the c axis, where the quintuple atomic layers are linked by weak van der Waals interaction (inset of Fig. 1). A natural question is how sensitive this material is to pressure. Indeed, the changes in the gap under pressure in the related compounds Bi₂Te₃ and Bi₂Se₃ suggest that hydrostatic pressure is very effective at tuning the band structure. In Bi₂Te₃, Vilaplana *et al.*⁴⁶ reported reducing the gap from 170 to 120 meV by applying 6 GPa. In Bi₂Se₃ the optical gap is increased from 170 meV at ambient pressure to 450 meV at 8 GPa.⁴⁷

In Fig. 5(a), $\log(1/t)$ is plotted as a function of frequency for different pressures at room temperature. Transmission through a thin film of thickness d is given by⁴⁸

$$t(\omega) \approx \frac{1}{1 + 4\pi d \sigma_1(\omega)/c} \quad (4)$$

so that $1/t$ represents an approximation to the real part of the conductivity, offset by a constant. The gap may be simply estimated as the energy at half of the maximum value of $1/t(\omega)$. The oscillations below the gap edge are caused by the Fabry-Perot interference, previously illustrated in Fig. 2(b). The pressure dependence of the gap may also be obtained from the reflectivity measurements, shown in Fig. 5(b). Below the gap edge, strong Fabry-Perot oscillations appear and the energy of their onset may be taken as the value of the gap. Figure 5(c) shows the pressure dependence of the gap determined from the transmission and reflectivity measurements as described above; the two estimates agree very well.

Up to 4 GPa, the effect of pressure on the gap edge in Bi₂Te₂Se is fairly modest, especially when compared to Bi₂Te₃ or Bi₂Se₃ (Refs. 46 and 47). However, a steep decrease

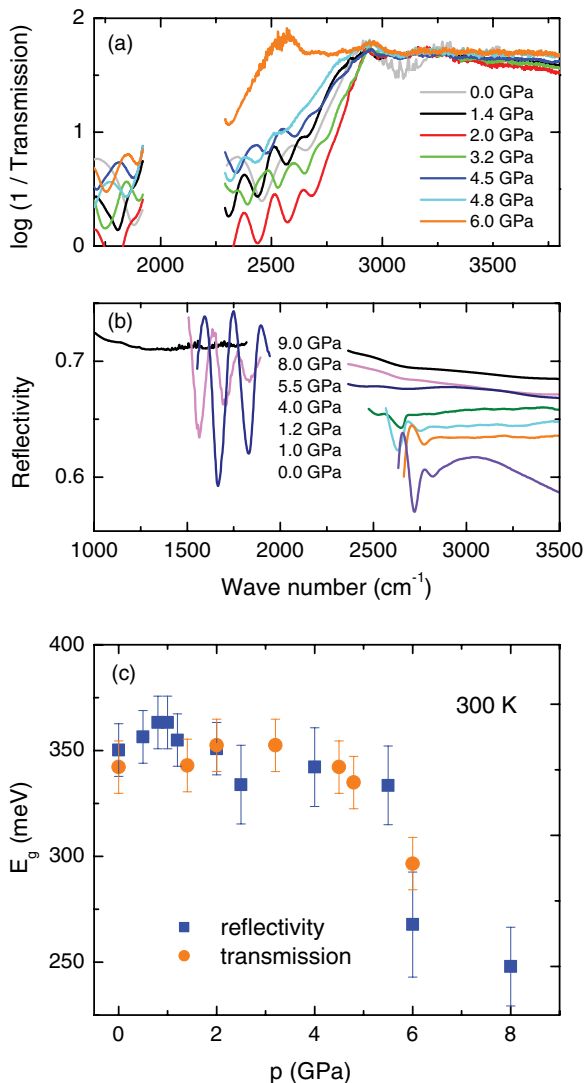


FIG. 5. (Color online) The frequency dependence at room temperature of (a) the log of the inverse transmission and (b) the reflectivity, for a thin flake of $\text{Bi}_2\text{Te}_2\text{Se}$ at various pressures. The spectral range between 2000–2300 cm^{-1} is not shown due to the strong absorptions of the diamond in this region. (c) The comparison of the pressure dependence of the bulk band gap E_g determined from reflectivity and transmission measurements.

in the gap value begins above 4 GPa, and by 8 GPa the gap has moved from ~ 340 to ~ 250 meV. A wider spectral range for the reflectivity measured under pressure is shown in Fig. 6. For clarity, only the data above ~ 2800 cm^{-1} are shown. Already below 1 GPa, the reflectivity changes significantly as pressure is applied. At the lowest pressures, up to 0.8 GPa, the two lowest interband transitions at ≈ 3000 and 5000 cm^{-1} are still distinguishable. As the pressure increases to 1.0 GPa, these two peaks merge into a single peak at ≈ 4000 cm^{-1} . When the pressure is further increased, the reflectivity level increases. Above $p \approx 9$ –10 GPa the gap can no longer be followed. Extrapolating the data in Fig. 5 the system is expected to become metallic above 10 GPa.

To compare our data with the band structure predictions, the inset of Fig. 7 shows a comparison between the experimentally

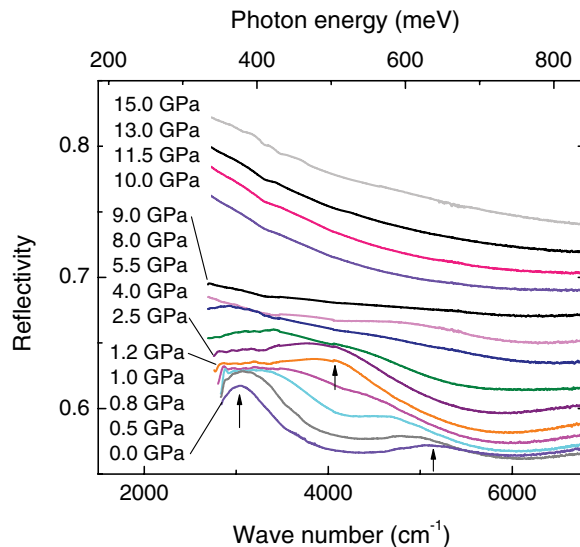


FIG. 6. (Color online) The detailed pressure dependence of the reflectivity of $\text{Bi}_2\text{Te}_2\text{Se}$ at room temperature. The arrows indicate the location of features associated with interband absorptions.

determined σ_1 at 5 K and the calculated σ_1 for an uncompressed lattice. Overall, the agreement is quite good and the value of the gap is approximately correct. The absorption bands are all reproduced, despite a minor shift in frequency.

The main panel of Fig. 7 shows the calculated conductivity σ_1 for different lattice compressions. The effect of pressure on this layered structure was simulated as a reduction of interplanar distances along the c axis while keeping the a - b plane lattice parameters constant. In this way we only change the distance between quintuple layers, linked by van der Waals interactions. All the other bonds are covalent and therefore much less compressible. The calculated gap edge does not significantly depend on c -axis compression. On the contrary, the absorptions above the gap edge, marked by arrows in Fig. 7, show pressure dependence. For 5% compression of the

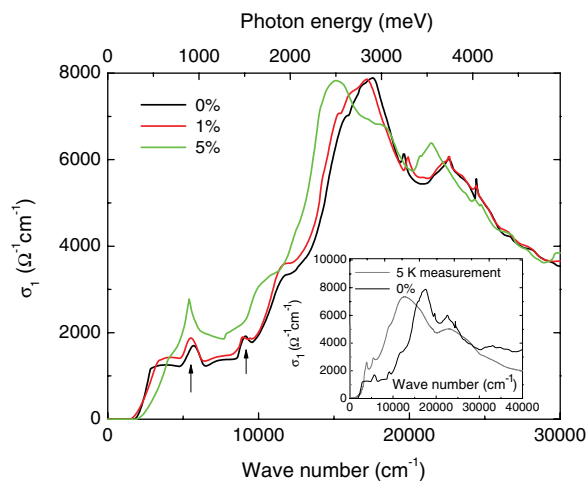


FIG. 7. (Color online) First-principles calculations (including spin-orbit coupling) of the real part of conductivity σ_1 for various lattice compressions along the c axis. Inset: Comparison of calculated σ_1 and the measured optical conductivity at 5 K at ambient pressure.

c axis, only one peak remains below 10 000 cm⁻¹. This agrees with the reflectivity under pressure, which shows that the two structures below 6000 cm⁻¹ merge into one for pressures above 1.0 GPa.

Overall, the high-pressure behavior of optical properties in Bi₂Te₂Se suggests that its band structure is very sensitive to pressure. The collapse of the gap does not seem to be captured by the LDA calculations in which only *c*-axis compression is considered. This indicates that the changes of the geometry within a quintuple layer may play an important role in the closing of the gap under pressure.

IV. CONCLUSION

The optical properties of Bi₂Te₂Se have been determined over a wide temperature and frequency range. The far-infrared optical conductivity indicates the presence of an impurity band at ≈ 200 cm⁻¹ (25 meV), well below the band gap. Numerous in-plane vibrational modes can be identified at 5 K in Bi₂Te₂Se, at least seven more than what is allowed by symmetry. Both the extra phonon modes and the impurity band are consistent with presence (and importance) of disorder and symmetry breaking in this material.

The band gap edge is determined to be $E_g \approx 300$ meV at room temperature. At low temperatures E_g shifts strongly to higher energies. Similarly, several interband transitions or absorptions above the gap edge show strong temperature dependence. Their behavior indicates that the band structure is significantly influenced by thermal contraction of the lattice.

The high-pressure optical properties of Bi₂Te₂Se have been determined at room temperature. A strong suppression of the gap edge occurs above 4.5 GPa. Commencing at low pressures, $p < 1.0$ GPa, absorptions above the gap edge show a strong pressure dependence. Our measurements are in reasonable agreement with LSDA calculations.

ACKNOWLEDGMENTS

We would like to thank Philip Allen and Alexey Kuzmenko for helpful discussions. Thanks are due to Alfredo Segura for very useful technical advice. Research was supported by the Swiss NSF through Grant No. 200020-135085 and its NCCR MaNEP. Work at BNL was supported by the U.S. Department of Energy, Office of Basic Energy Sciences, Division of Materials Sciences and Engineering under Contract No. DE-AC02-98CH10886. A.A. acknowledges funding from “Boursières d’Excellence” of the University of Geneva.

*ana.akrap@unige.ch

†homes@bnl.gov

¹D. Hsieh, D. Qian, L. Wray, Y. Xia, Y. S. Hor, R. J. Cava, and M. Z. Hasan, *Nature (London)* **452**, 970 (2008).

²M. Z. Hasan and C. L. Kane, *Rev. Mod. Phys.* **82**, 3045 (2010).

³J. E. Moore, *Nature (London)* **464**, 194 (2010).

⁴H. Zhang, C.-X. Liu, X.-L. Qi, X. Dai, Z. Fang, and S.-C. Zhang, *Nat. Phys.* **5**, 438 (2009).

⁵L.-L. Wang and D. D. Johnson, *Phys. Rev. B* **83**, 241309 (2011).

⁶M. Z. Hasan, H. Lin, and A. Bansil, *Physics* **2**, 108 (2009).

⁷T. Valla, Z.-H. Pan, D. Gardner, Y. S. Lee, and S. Chu, *Phys. Rev. Lett.* **108**, 117601 (2012).

⁸E. Gaudin, S. Jobic, M. Evain, and R. Brec, *Mater. Res. Bull.* **30**, 549 (1995).

⁹N. K. Abrikosov and V. F. Barkina, *Zh. Neorg. Khim.* **3**, 659 (1958).

¹⁰C. B. Satterthwaite and R. W. Ure, *Phys. Rev.* **108**, 1164 (1957).

¹¹V. Kul’bachinskii, A. Kaminskii, K. Kindo, Y. Narumi, K. Suga, P. Lostak, and P. Svanda, *JETP Lett.* **73**, 352 (2001).

¹²A. Sklenár, C. Drasar, A. Krejcová, and P. Losták, *Cryst. Res. Technol.* **35**, 1069 (2000).

¹³T. Plecháček, J. Navrátil, and J. Horák, *J. Solid State Chem.* **165**, 35 (2002).

¹⁴Z. Ren, A. A. Taskin, S. Sasaki, K. Segawa, and Y. Ando, *Phys. Rev. B* **82**, 241306(R) (2010).

¹⁵S. Jia, H. Ji, E. Climent-Pascual, M. K. Fuccillo, M. E. Charles, J. Xiong, N. P. Ong, and R. J. Cava, *Phys. Rev. B* **84**, 235206 (2011).

¹⁶Z. Ren, A. A. Taskin, S. Sasaki, K. Segawa, and Y. Ando, *Phys. Rev. B* **85**, 155301 (2012).

¹⁷J. Xiong, A. Petersen, D. Qu, Y. Hor, R. Cava, and N. Ong, *Physica E* **44**, 917 (2012).

¹⁸H. Ji, J. M. Allred, M. K. Fuccillo, M. E. Charles, M. Neupane, L. A. Wray, M. Z. Hasan, and R. J. Cava, *Phys. Rev. B* **85**, 201103(R) (2012).

¹⁹M. Neupane, S.-Y. Xu, L. A. Wray, A. Petersen, R. Shankar, N. Alidoust, C. Liu, A. Fedorov, H. Ji, J. M. Allred, Y. S. Hor, T.-R. Chang, H.-T. Jeng, H. Lin, A. Bansil, R. J. Cava, and M. Z. Hasan, *Phys. Rev. B* **85**, 235406 (2012).

²⁰T. Arakane, T. Sato, S. Souma, K. Kosaka, K. Nakayama, M. Komatsu, T. Takahashi, Z. Ren, K. Segawa, and Y. Ando, *Nature Commun.* **3**, 636 (2012).

²¹H. Köhler and C. R. Becker, *Phys. Status Solidi B* **61**, 533 (1974); K. Unkelbach, C. Becker, H. Köhler, and A. Middendorff, *ibid.* **60**, K41 (1973).

²²A. D. LaForge, A. Frenzel, B. C. Pursley, T. Lin, X. Liu, J. Shi, and D. N. Basov, *Phys. Rev. B* **81**, 125120 (2010).

²³P. Di Pietro, F. M. Vitucci, D. Nicoletti, L. Baldassarre, P. Calvani, R. Cava, Y. S. Hor, U. Schade, and S. Lupi, *Phys. Rev. B* **86**, 045439 (2012).

²⁴S. Nakajima, *J. Phys. Chem. Solids* **24**, 479 (1963).

²⁵P. Bayliss, *Am. Mineral.* **76**, 257 (1991).

²⁶C. C. Homes, M. Reedyk, D. A. Crandles, and T. Timusk, *Appl. Opt.* **32**, 2976 (1993).

²⁷M. Dressel and G. Grüner, *Electrodynamics of Solids* (Cambridge University Press, Cambridge, England, 2001).

²⁸F. Wooten, *Optical Properties of Solids* (Academic, New York, 1972), pp. 244–250.

²⁹F. Datchi, A. Dewaele, P. Loubeyre, R. Letoulllec, Y. Le Godec, and B. Canny, *High Press. Res.* **27**, 447 (2007).

³⁰P. Lerch, L. Quaroni, J. Wambach, J. Schneider, D. Armstrong, D. Rossetti, F. Mueller, P. Peier, V. Schlott, L. Carroll, P. Friedli, H. Sigg, S. Stutz, and M. Tran, *J. Phys.: Conf. Ser.* **359**, 012003 (2012).

- ³¹S. Y. Savrasov, *Phys. Rev. B* **54**, 16470 (1996).
- ³²J. P. Perdew, K. Burke, and M. Ernzerhof, *Phys. Rev. Lett.* **77**, 3865 (1996).
- ³³P. Larson, V. A. Greanya, W. C. Tonjes, R. Liu, S. D. Mahanti, and C. G. Olson, *Phys. Rev. B* **65**, 085108 (2002).
- ³⁴X.-Q. Dai, B. Zhao, J.-H. Zhao, Y.-H. Li, Y.-N. Tang, and N. Li, *J. Phys.: Conf. Ser.* **24**, 035502 (2012).
- ³⁵A. Akrap, A. Ubaldini, E. Giannini, and L. Forró, arXiv:1210.3901v1.
- ³⁶G. E. Jellison and F. A. Modine, *Appl. Phys. Lett.* **69**, 371 (1996); **69**, 2137 (1996).
- ³⁷A. Kuzmenko, computer code REFFIT, University of Geneva, Geneva, Switzerland.
- ³⁸P. Lautenschlager, P. B. Allen, and M. Cardona, *Phys. Rev. B* **31**, 2163 (1985).
- ³⁹A. Gaymann, H. P. Geserich, and H. v. Löhneysen, *Phys. Rev. B* **52**, 16486 (1995).
- ⁴⁰W. Richter and C. R. Becker, *Phys. Status Solidi B* **84**, 619 (1977).
- ⁴¹W. Cheng and S.-F. Ren, *Phys. Rev. B* **83**, 094301 (2011).
- ⁴²C. C. Homes, T. Timusk, D. A. Bonn, R. Liang, and W. N. Hardy, *Can. J. Phys.* **73**, 663 (1995).
- ⁴³M. J. Rice, *Phys. Rev. Lett.* **37**, 36 (1976).
- ⁴⁴C. S. Jacobsen, D. B. Tanner, and K. Bechgaard, *Phys. Rev. B* **28**, 7019 (1983).
- ⁴⁵M. Reedyk and T. Timusk, *Phys. Rev. Lett.* **69**, 2705 (1992).
- ⁴⁶R. Vilaplana, O. Gomis, F. J. Manjón, A. Segura, E. Pérez-González, P. Rodríguez-Hernández, A. Muñoz, J. González, V. Marín-Borrás, V. Muñoz-Sanjose, C. Drasar, and V. Kucek, *Phys. Rev. B* **84**, 104112 (2011); R. Vilaplana, D. Santamaría-Pérez, O. Gomis, F. J. Manjón, J. González, A. Segura, A. Muñoz, P. Rodríguez-Hernández, E. Pérez-González, V. Marín-Borrás, V. Muñoz-Sanjose, C. Drasar, and V. Kucek, *ibid.* **84**, 184110 (2011).
- ⁴⁷A. Segura, V. Panchal, J. F. Sánchez-Royo, V. Marín-Borrás, V. Muñoz-Sanjose, P. Rodríguez-Hernández, A. Muñoz, E. Pérez-González, F. J. Manjón, and J. González, *Phys. Rev. B* **85**, 195139 (2012).
- ⁴⁸E. van Heumen and D. van der Marel, in *Lectures on the Physics of Strongly Correlated Systems XI: Eleventh Training Course in the Physics of Strongly Correlated Systems, 2006*, edited by F. Mancini and A. Avella, AIP Conference Proceedings 918 (American Institute of Physics, Melville, NY, 2007).